A comparison of pendulum experiments and discrete-element simulations of oblique collisions of wet spheres

Oscar Punch[1], Megan Danczyk[1], Mathew Hawken[1], and Daniel J. Holland[1,*]

[1]Department of Chemical and Process Engineering, University of Canterbury, New Zealand

[*]mailto: daniel.holland@canterbury.ac.nz

Abstract

Oblique collisions of two spherical particles coated with a thin layer of viscous liquid are considered. Experimental measurements are performed using particle tracking velocimetry. Comprehensive experimental data for collisions with an impact angle between 0°- 60°are presented. Collisions are characterised by the Stokes' number, the coefficient of restitution, and the rotational velocity. The experiments are compared to numerical simulations using the discrete element method (DEM). The translational velocities predicted by the simulations were in good agreement with the experiments at high Stokes' number, where the models are dominated by the normal components. As the tangential forces become more significant (i.e. at low to medium Stokes' number, and high collision angle), agreement between the simulations and experiments is poorer. At low Stokes' number the translational velocities were in good agreement with the experiments, but was poorer at high Stokes' number.

1 Introduction

Recent studies have shown that the discrete-element method (DEM) is a powerful tool for simulating dry granular mixtures [1, 2]; however, the extension of DEM to wet granular mixtures has proved challenging [3, 4, 5]. Several studies have concluded that the inclusion of even small amounts of liquid, drastically change the rheology of the granular flow [6]. Many studies have investigated the macroscopic nature of these wet granular flows [3, 7, 8], however little study has been conducted on the microscopic dynamics of collisions of wet particles. The vast majority of the work on wet granular flows has used non-viscous liquids where capillary forces dominate and viscous forces can be considered negligible [9, 10, 11, 12]. However, in processes such as polymer coating the viscous forces dominate. Here we consider oblique collisions of

spherical particles coated in thin layers of viscous liquid such that viscous forces will dominate but capillary forces may be significant at low velocity.

The regime we consider has a thin layer of interstitial liquid between the spheres. The interstitial liquid between the spheres during the collision forms a pendular bridge and we refer to these systems as being in the pendular regime [13]. As two spheres approach one another, they displace the interstitial liquid and viscous forces act to slow the approach [14]. The fluid also generates capillary forces, which act inwards towards the center of the spheres [15]. A modified Capillary number, Ca, is used to determine the ratio of viscous forces to capillary forces [16].

$$Ca = \frac{3\mu \vec{v}^{n}_{ij,0} r_{ij}}{\sigma h_{ij,0}} \tag{1}$$

Here, μ is the viscosity of the interstitial liquid, $\vec{v}^{n}_{ij,0}$ is the relative pre-collisional velocity in the normal direction, r_{ij} is the reduced radius, $r_{ij} = (r_1 r_2)/(r_1 + r_2)$, σ is the surface tension of the interstitial liquid, and $h_{ij,0}$ is the initial liquid film thickness. Studies on linear collisions in the pendular regime have stated that capillary forces can be considered negligible if $Ca > 1000$ [17]. However, some studies have found that capillary forces are significant for oblique collisions [18] and thus they will be considered in this study despite Ca ≈ 1000 at the lowest considered velocities. Previous studies have also found that the collisions are well characterised by two dimensionless parameters: the normal Stokes number, St^n, a ratio of inertial forces to viscous forces in the normal direction, and the normal coefficient of restitution, e^n, a ratio of the outgoing kinetic energy to the incoming kinetic energy in the normal direction [2, 16, 19].

$$St^n = \frac{m_{ij} \vec{v}^{n}_{ij,0}}{6\pi\mu r_{ij}^2} \tag{2}$$

$$e^n = -\frac{\sum \vec{v}_{ij,f} \cdot \vec{n}_f}{\sum \vec{v}_{ij,0} \cdot \vec{n}_0} \tag{3}$$

Here, m_{ij} is the reduced mass, $m_{ij} = (m_1 m_2)/(m_1 + m_2)$, $\vec{v}_{ij,f}$ is the final relative velocity of the spheres, $\vec{n}_f$ is the normal vector at the time of final relative velocity, and $\vec{n}_0$ is the initial normal vector. Empirical studies have found good correlations between these dimensionless numbers and viscous force models for normal collisions [19, 20, 21].

Experimental measurements of oblique collisions of wet granular flows include both particle-wall [20, 22], and particle-particle [18] contacts. Here we focus on oblique collisions between two wetted particles, for which Donahue et al. made some critical observations [18]. They found that there are three possible outcomes for an oblique collision of two wetted spheres: *stick-rotate*, the spheres do not have sufficient inertial forces to separate and instead rotate about one another, *stick-rotate-separate*, the spheres have sufficient inertial

forces during rotation to separate after some angle has been rotated through, and *contact-bounce*, the spheres have sufficient normal force that they separate near-instantaneously and negligible rotation occurs about one another. In both of the last outcomes the angular velocity of the spheres changes as a result of the collision. Donahue et al. did not report any rotational velocities in their study. However, the rotational velocity of a sphere contacting a wet plate has been considered by Buck et al. who found that the normal coefficient of restitution was independent of pre-collisional rotation [20]. To the best of our knowledge, the rotational velocity of the spheres has not been reported for sphere-sphere contact.

DEM models have been used to describe the collisions of liquid coated particles that are comprised of both viscous and capillary forces [23]. Viscous force models are derived from Reynolds lubrication theory [24, 25]. Some viscous force models assume the surface of two contacting spheres is flat [14], whilst others have considered the curvature of the contacting surfaces [20, 26]. In all models, as the gap between two spheres tends towards zero, the viscous force tends towards infinity. Thus, a minimum separation distance is implemented to cap the viscous force. The most widely used model caps the minimum separation at an arbitrary value. This value may be related to the surface roughness of the spheres [7], but that has not been confirmed. This model has been extended by several authors to investigate the effect of considering the liquid forces only when solid-solid contact has occurred [27] or as soon as the liquid films overlap [28]. Another viscous force model does not impose a constant value on the minimum separation distance; instead it is assumed that the interstitial liquid undergoes a glass-transition and the minimum separation distance is velocity dependent [16, 17]. Despite the good agreement of this glass-transition model, it is not widely used.

A recent study showed that for a normal viscous force model to be representative of a normal collision between two spherical particles in the pendular regime there are two things which must be considered: the curvature of the spheres, and a variable minimum separation distance [23]. Using a scaling parameter, good agreement between between these viscous force models and experimental linear collisions is found [16, 17, 29]. However, the agreement between viscous force models and oblique collisions is poor [18, 26]. Furthermore, it is challenging to test oblique viscous force models due to the lack of comprehensive experimental data.

It is theorised there must be some form of solid-solid contact occurring, otherwise the spheres would agglomerate. However, it is not clear how this solid-solid interaction occurs. Three prevailing theories have been proposed: the liquid solidifies and acts as a medium for a solid-solid contact to occur [16], the solids deform sufficiently that the elasticity causes a solid-solid like contact to occur [19], or there is physical solid-solid contact between the surfaces of the spheres [7]. If physical solid-solid contact is occurring, friction may be important in describing the post-collisional rotation. However, many studies assume a coefficient of friction equal to zero for viscous force dominated systems [21, 28]. Friction was considered by Davis

and Sitison and found to increase rotational velocity once solid-like contact has occurred [26]; however, no comparison to experiments was made.

In this study, experiments are conducted using a modified Newton's cradle setup where two spheres are each suspended from a single point such that they can rotate about themselves and each other. One of these spheres is coated in a viscous liquid and collisions measured at a variety of velocities and angles. The experiments are then used to examine recent viscous force models using DEM.

2 Theory

An overview of the theory used to describe an oblique collision of wetted spherical particles via viscous and capillary force models is presented. The implementation of these viscous and capillary force models to DEM is also considered.

2.1 Discrete element modelling

DEM uses Newton's laws of motion to describe particle motion. In this study, a soft-sphere DEM implementation using the open-source software LIGGGHTS$^{\mathrm{TM}}$ was used [30]. For a particle, i, the translational and rotational motion are given by:

$$m_i \frac{d\vec{v}_i}{dt} = \sum_j [(\vec{F}^n_{ij} + \vec{F}^n_{cap,ij} + \vec{F}^n_{visc,ij}) + (\vec{F}^t_{ij} + \vec{F}^t_{visc,ij})] \tag{4}$$

$$I_i \frac{d\omega_i}{dt} = \sum_j [r_i(\vec{F}^t_{ij} + \vec{F}^t_{visc,ij} + \vec{T}_{r,ij})] \tag{5}$$

where $\vec{v}_i$ is the translational velocity of the i$^{\mathrm{th}}$ particle. The forces during a collision are represented by the solid contact force, $\vec{F}_{ij}$, capillary force, $\vec{F}_{cap,ij}$, and the viscous force, $\vec{F}_{visc,ij}$ for their respective normal F^n, or tangential F^t components. The rotational velocity, ω_i, is described by the tangential forces, and a torque due to the rolling friction, $\vec{T}_{i,r}$. Here, $\vec{T}_{i,r} = 0$ and will not be considered. Several authors have stated that capillary forces may be significant for oblique collisions, despite a high capillary number $Ca > 1000$ [18][26], so they will be included in this study. It should be noted that $\vec{F}_{cap,ij}$ only acts in the normal direction.

A solid-solid contact model is used in DEM when the solid surfaces intersect. For this study we use the Hertz-Mindlin contact model which is given below.

$$\vec{F}_{ij} = \underbrace{(k^n \vec{\delta}^n_{ij} - \gamma^n \vec{v}^n_{ij})}_{\text{normal force}} + \underbrace{(k^t \vec{\delta}^t_{ij} - \gamma^t \vec{v}^t_{ij})}_{\text{tangential force}} \tag{6}$$

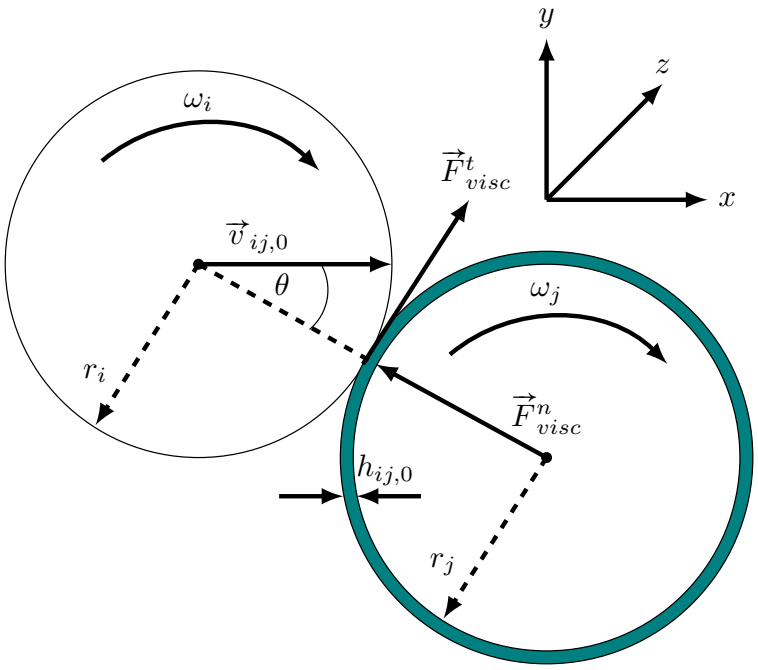

Figure 1: An oblique collision schematic where the striking particle has contacted the stationary particle at angle θ with relative velocity v^0_{ij}.

Here, k is the elastic constant, $\vec{\delta}$ is the overlap distance of two particles, and γ is the viscoelastic damping, again each of these has both normal n and tangential t components. Further description of the Hertz-Mindlin model is available in the LIGGGHTS$^{\text{TM}}$ documentation [30].

2.2 Liquid contact forces

A schematic of two spheres approaching each other at an angle is shown in Fig. 1. One of these spheres is coated with a viscous liquid. The viscous force model for two approaching spheres with interstitial liquid is derived from Reynolds' lubrication theory [24, 25]. While there are several viscous force models [16, 27, 28], a recent study found that it is critical to include the curvature of the spheres for linear collisions of liquid coated spheres [23]. Only two normal viscous force models consider the curvature of the spheres, a static liquid bridge model [31] (here referred to as SB) and a deforming bridge model [26] (here referred to as DB). The SB model assumes the displaced interstitial liquid does not influence the viscous force, whereas the DB model includes a simple model of the liquid displacement. As these two models are the only normal viscous force model which consider the curvature of the spheres, they are the only models that will be studied here. Two tangential viscous force models will be considered: a model by Davis [26] and a model by Nase et al. [7]. The tangential viscous force expression given by Nase et al. was originally derived by O'Neill for fully immersed spheres [32] and then solved numerically by Goldman et al. [33]. Previous studies have not

considered the effect of different tangential viscous force models. The viscous force models are given by,

$$\vec{F}^{n}_{visc,SB} = \frac{6\pi\mu a^2 \vec{v}^{n}}{h_{ij}}[1 - h_{ij}/(h_{max})]^2 \tag{7}$$

$$\vec{F}^{n}_{visc,DB} = \frac{6\pi\mu a^2 \vec{v}^{n}}{h_{ij}}[1 - h_{ij}/(2h_{max} - h_{ij})]^2 \tag{8}$$

$$\vec{F}^{t}_{visc,Davis} = 2\pi\mu a \vec{v}^{t} \ln[(2h_{max} - h_{ij})/h_{ij}] \tag{9}$$

$$\vec{F}^{t}_{visc,Nase} = 6\pi\mu a \vec{v}^{t}(\frac{8}{15} ln \frac{a}{h_{ij}} + 0.9588) \tag{10}$$

where h_{max} is the sum of the film thickness on both spheres at $t = 0$. It is assumed that this is the maximum film thickness possible pre- and post-collision. Once the distance between the spheres exceeds h_{max}, the spheres do not experience any viscous force.

A key limitation of these viscous force models is that as the separation distance between spheres approaches 0, the viscous force tends towards infinity [7, 17]. Therefore, a minimum separation distance must be implemented to ensure simulation stability; this is referred to as h_{min}. In previous research it was assumed that a hard-sphere collision occurred at h_{min} [26]. However, this approach is not compatible with the more general soft-sphere DEM framework used here. Instead, it is assumed that if $h_{min} > h_{ij}$ the viscous force is kept either constant or near-constant. Two implementations of constant viscous force are considered here: firstly, the case where the viscous force is assumed to be negligible during the solid-solid contact and hence $\vec{F}_{visc} = 0$ when $h_{min} > h_{ij}$, and secondly the case where $\vec{F}_{visc}$ is held near-constant by setting $h_{ij} = h_{min}$ when $h_{min} > h_{ij}$. It has been shown that a soft-sphere model with $\vec{F}_{visc} = 0$ when $h_{min} > h_{ij}$ achieves comparable results to the original implementation that used a hard-sphere collision [23]. However, this approach may not be feasible for simulations of larger systems with DEM as it could cause numerical instability due to agglomerated particles going from $\vec{F}_{visc} = 0$ to much higher forces if they contact other particles. Therefore, we have also considered the second case where $\vec{F}_{visc}$ is kept near-constant, but non-zero, when $h_{min} > h_{ij}$. These various implementations of constant and near-constant viscous force will henceforth be referred to as $\vec{F}_{visc,C}$ and $\vec{F}_{visc,NC}$, respectively. To concisely describe the many implementations of the viscous force equations we introduce a new parameter, $\vec{F}^{k}_{visc,mod}$ which describes any type of viscous force equation (normal or tangential) and is given in Eq. 11.

$$\vec{F}^{k}_{visc,mod,l} = f(\vec{v}^{k}, h) \tag{11}$$

Here, k represents either the normal or tangential viscous force, and l is either the constant (C) or near-constant (NC) form of the viscous force equation. The cases for which F_{visc} changes as h_{ij} changes are then

described by:

$$\vec{F}^k_{visc,C} = \begin{cases} 0 & h_{ij} > h_{max} \\ \vec{F}^k_{visc,mod}(\vec{v}^k, h_{ij}) & h_{max} \geq h_{ij} \geq h_{min} \\ 0 & h_{min} > h_{ij} \end{cases} \tag{12}$$

$$\vec{F}^k_{visc,NC} = \begin{cases} 0 & h_{ij} > h_{max} \\ \vec{F}^k_{visc,mod}(\vec{v}^k, h_{ij}) & h_{max} \geq h_{ij} \geq h_{min} \\ \vec{F}^k_{visc,mod}(\vec{v}^k, h_{min}) & h_{min} > h_{ij} \end{cases} \tag{13}$$

To describe h_{min} we use a model proposed by Donahue et al. [16] which suggests that if the pressure build up in the liquid is sufficiently high, the liquid can undergo a glass-transition and h_{min} is given by Eq. 14,

$$h_{min} = \begin{cases} h_{max} & h_{min} \geq h_{max} \\ (3\mu r_{ij} \vec{v}^n_{ij} / P_{gt})^{1/2} & h_{min} < h_{max} \end{cases} \tag{14}$$

where P_{gt} is the glass-transition pressure of the interstitial liquid. For collisions of arbitrarily fast spheres, h_{min} will eventually exceed h_{max}. Therefore, the condition that $h_{min} = h_{max}$ if $h_{min} \geq h_{max}$ has been implemented. From Eq. 14 it can be seen that h_{min} scales with $(\vec{v}^n)^{1/2}$. However, as the collision angle increases, $\vec{v}^n$ will decrease and therefore h_{min} will decrease. At the same time, the tangential velocity $\vec{v}^t$ increases. Here it is assumed that the tangential velocity does not impact h_{min} and that h_{min} is determined by the normal velocity only.

This study will also consider the capillary force. A capillary force model proposed by Davis is used, which is given by Eq. 15 [26].

$$\vec{F}_{cap} = -8\pi r_{ij} \sigma \tag{15}$$

The capillary force is a cohesive force which acts towards the center of the interstitial liquid and therefore only acts in the normal direction. Selected tests were also performed using the capillary force of Nase et al. [7], and comparable results were obtained (not shown). For derivation of the viscous and capillary forces please see [26].

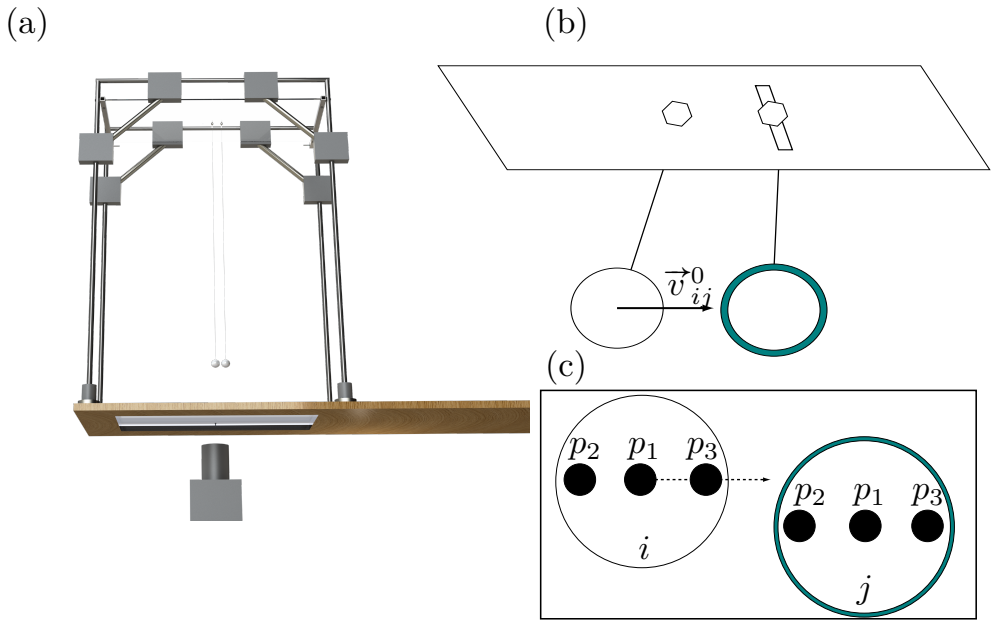

Figure 2: Perspectives of the Stokes' cradle setup: (a) is a render of the setup, (b) is a schematic of the top down view of the setup, and (c) is a schematic of the camera view.

3 Methods

3.1 Modified Newton's cradle setup

The experimental setup is shown in Fig. 2 and was based on the Stokes' cradle setup which has seen success with similar studies [16, 18][23]. In this study we use two stainless steel spheres 25.4 mm (1 in.) in diameter. In a prior study, the roughness of the spheres was measured to be < 1 μm, and the dry coefficient of restitution for the spheres was measured to be 0.90 ± 0.05 [23]. The spheres are suspended from a single point, by 1 m long 20 lb. nylon fishing line, to ensure the spheres can freely rotate about each other and themselves. The long string length is used to minimise the curvature of the path of the spheres that occurs due to the pendulum motion. The single suspension point is on a slider which can be moved perpendicular to the striking arc of the sphere, to change the angle of collision. In this study a single camera is placed underneath the spheres and the collisions are imaged through an acrylic plate.

Prior to collision, the stationary sphere is fully immersed in 10 Pa.s silicone oil and left to drip for three minutes. After three minutes, the film thickness corresponds to $h_{max} = 270$ μm, as quantified in previous work [23]. At three minutes, the camera begins recording and the striker sphere is released. Prior to each collision, the striker sphere is placed an arbitrary distance away from the stationary sphere to ensure a range of striking velocities is investigated. The contact angles investigated range between 0° and 60° at intervals of 15°. All experimentally reported contact angles are within ± 5° of their associated contact angle group. The

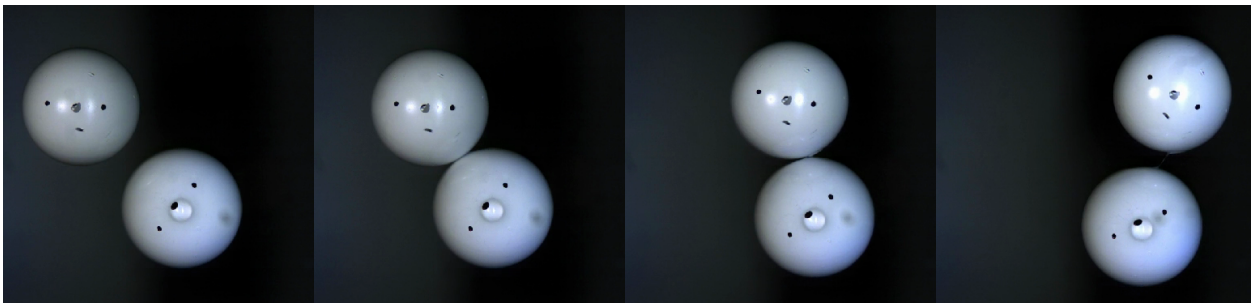

Figure 3: Example images obtained from the high-speed imaging for a stick-rotate-separate collision at 45° and $St^n = 1.38$.

collision is considered finished if the spheres reverse direction due to reaching the apex of their pendulum motion, or if they have rotated about one another such that the strings cross.

The collisions are recorded using a Photron SA-5 high speed camera with a Tamron SP AF Aspherical XR lens. The collisions are imaged at 5000 frames per second with a focal length of 75 mm, and an aperture of f/5.6. To resolve the translational and rotational motion of the spheres, three equidistant tracking dots are painted on the bottom of the spheres with one dot directly in-line with the suspension string. An example of the images obtained from the recording for a stick-rotate-separate case is shown in Fig. 3. The displacement of the dots is found using the particle tracking velocimetry program GOM Correlate®. The dry striker sphere is used to calibrate the resolution of the images. The resolution was found to be ≈ 175 μm/pixel. The distance travelled per frame at 5000 FPS is significantly less than 175 μm, hence it is challenging to resolve the velocity accurately. We considered imaging at a lower frame rate to increase the displacement between frames, but this reduced the ability to resolve the time of the collision, which is required to determine the angle of impact precisely. Instead, a feature correlation method in GOM Correlate is used to track the motion with a sub-pixel resolution. The velocity was then obtained using a 2^{nd} order Savitsky-Golay filter with filter length of 7 frames to further reduce the noise in position tracking. The combination of the filter and feature correlation methods enabled accurate measurement of the velocity and the angle of impact.

3.2 Resolving translational and rotational velocity

To track the motion of the spheres, we consider the three dots on the bottom of the spheres, as seen in Fig. 2(c). The position of the dots in Cartesian coordinates follows the form $p^i_{j,k}$ where i is the time step at which the coordinates occur, j is the type of coordinate (i.e. x or y), and k is the number of the dot being described. The outer dots, at p_2 and p_3, and their relative position in sequential images, to the central dot, at p_1, are used to determine the translational and rotational velocity of the spheres. For a two sphere collision, the angle of impact is given by the absolute position of the central dots for each sphere from each

other. At the moment before collision, the impact angle, θ, is given by,

$$\theta = \tan^{-1} \frac{p^i_{y,1,\text{static particle}} - p^i_{y,1,\text{striking particle}}}{p^i_{x,1,\text{static particle}} - p^i_{x,1,\text{striking particle}}} \tag{16}$$

The coordinates of p_1 are not impacted by rotational velocity and therefore the change in position of p_1 between two time steps is given by,

$$p^{i+1}_{x,1} - p^i_{x,1} = v_x \Delta t \tag{17}$$

$$p^{i+1}_{y,1} - p^i_{y,1} = v_y \Delta t \tag{18}$$

where Δt is the time between frames. To account for the arbitrary orientation of the sphere, the rotational velocity term is determined from the difference in position between $\mathbf{p}_1$ and $\mathbf{p}_2$ (or p_3). Rotation of the particle will cause a sinusoidal change in position. To simplify the calculation and create a linear system of equations, a small angle approximation is used such that the displacement in x due to rotation is given by $dx = -Rsin\alpha \approx -R\alpha$ where R is the distance between the central dot and outer dot, i.e. $|\mathbf{p}^i_1 - \mathbf{p}^i_2|$ and α represents the angle rotated by the outer dots in a single time step and is therefore given by $\omega\Delta t$, where ω is the rotational velocity of the sphere. The change in position of the outer dots can therefore be described by,

$$p^{i+1}_{x,2} - p^i_{x,2} = v_x \Delta t - \omega \Delta t (p^i_{y,1} - p^i_{y,2}) \tag{19}$$

$$p^{i+1}_{y,2} - p^i_{y,2} = v_y \Delta t + \omega \Delta t (p^i_{x,1} - p^i_{x,2}) \tag{20}$$

$$p^{i+1}_{x,3} - p^i_{x,3} = v_x \Delta t - \omega \Delta t (p^i_{y,2} - p^i_{y,3}) \tag{21}$$

$$p^{i+1}_{y,3} - p^i_{y,3} = v_y \Delta t + \omega \Delta t (p^i_{x,2} - p^i_{x,3}) \tag{22}$$

A full derivation of Eq. 19 – Eq. 22 is given in Appendix A. Eq. 17 – Eq. 22 can be represented in matrix form, $Ax = b$ where A is the time step components, x is the velocity components, and b is the position data

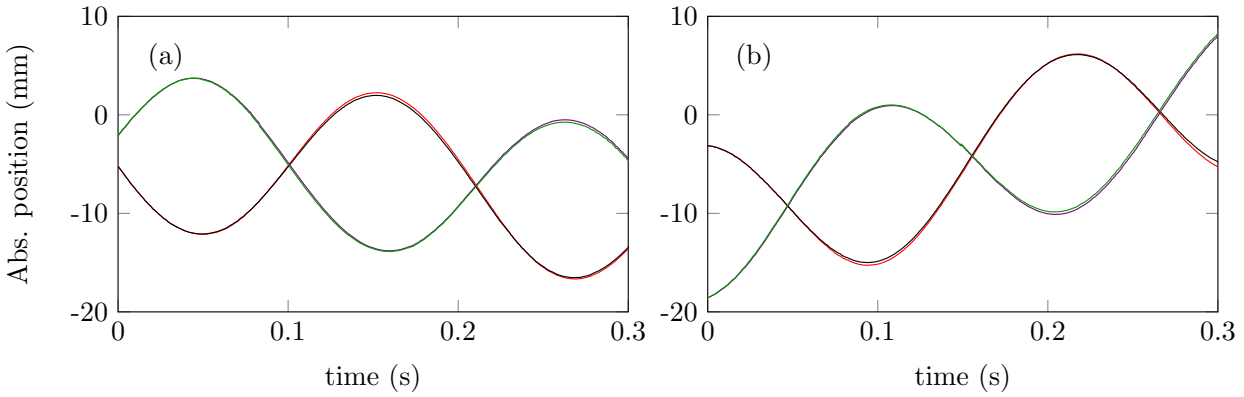

Figure 4: Absolute position for the tracking dots in the (a) x-direction, and (b) y-direction. The lines correspond to: $p_{i,2}$ calculated (—), $p_{i,2}$ GOM (—), $p_{i,3}$ calculated (—), and $p_{i,3}$ GOM (—).

of the dots. The resulting matrices follow the form,

$$A = \begin{bmatrix} \Delta t & 0 & 0 \\ 0 & \Delta t & 0 \\ \Delta t & 0 & -\Delta t(p^i_{y,1} - p^i_{y,2}) \\ 0 & \Delta t & \Delta t(p^i_{x,1} - p^i_{x,2}) \\ \Delta t & 0 & -\Delta t(p^i_{y,1} - p^i_{y,3}) \\ 0 & \Delta t & \Delta t(p^i_{x,1} - p^i_{x,3}) \end{bmatrix}, x = \begin{bmatrix} v_x \\ v_y \\ \omega \end{bmatrix}, b = \begin{bmatrix} p^{i+1}_{x,1} - p^i_{x,1} \\ p^{i+1}_{y,1} - p^i_{y,1} \\ p^{i+1}_{x,2} - p^i_{x,2} \\ p^{i+1}_{y,2} - p^i_{y,2} \\ p^{i+1}_{x,3} - p^i_{x,3} \\ p^{i+1}_{y,3} - p^i_{y,3} \end{bmatrix} \tag{23}$$

and are solved by the least squares method, where $x = (A'A)^{-1}(A'b)$, and A' is the transpose of A.

To validate the small angle approximation model we measure the rotational velocity of a single sphere with high ω experimentally. By visually timing the rotation of the particle from the high speed camera images, the rotational velocity was determined to be 30 rad/s. The images were then analysed using GOM Correlate and the absolute positions of the dots from GOM were used with the small angle approximation model to measure v_x, v_y, and ω. The measured rotational velocity using the solutions to Eq. 23 was 29.3 rad/s, which is in good agreement with that measured visually. These velocities are then used, again with the small angle approximation, to recalculate the positions and compare to the positions initially extracted from GOM. Fig. 4 shows the comparison of the positions output from GOM and the positions calculated after using the small angle approximation to determine the velocity components. From Fig. 4 it can be seen there is negligible difference between the position predicted by the small angle approximation, and the position output from GOM. As the small angle approximation model has held for large ω, it is assumed it will hold for smaller ω, where the angular change in position will be smaller.

An example of the translational and rotational velocity components obtained using this model for tracking

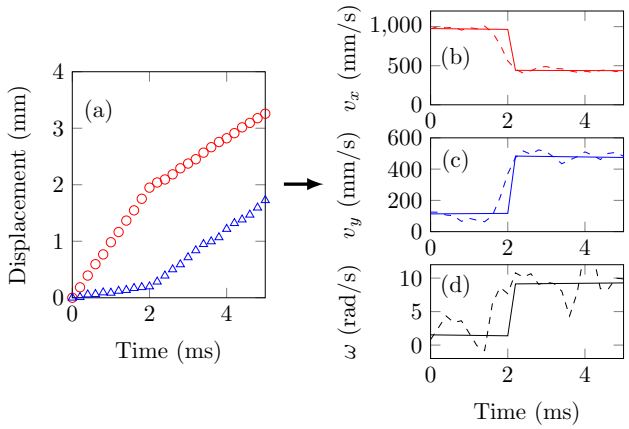

Figure 5: Resulting plots of particle velocimetry tracking for the striking particle of a 45° collision at $St^n = 3.08$. (a) is the raw position data in the x-direction (○) and y-direction (△). The plots (b), (c), and (d) show the velocity vectors extracted from (a) in the form of v_x, v_y, and ω, respectively. The dashed lines show the velocity at each time step extracted from the displacement data and the complete lines show the straight lines fit to the data.

an oblique collision between two particles is shown in Fig. 5. The displacement with time is nearly linear until the collision, which occurs at 2 ms. The duration of the collision is short when compared with the frame rate of the high speed camera, indicating that the collision lasts < 0.4 ms. It is possible that the liquid film contact occurs over a longer time than this estimate of the collision duration, however if that is the case the sphere does not slow sufficiently that the change in velocity can be detected. The velocities extracted from these displacement data show a rapid change at the time of the collision. The displacement between frames is small compared with the resolution of the images, so the measured velocity is oscillatory. However, before and after the collision, the velocity is nearly constant over the imaged region. Therefore, the velocity immediately before and after the collision was obtained by fitting a straight line to the measured velocity data before and after the collision. The collision time was defined as the time at which the velocity of the striking sphere has changed by > 50 mm/s. The velocity was taken as the value of these straight lines at the time 5 time steps (0.001 s) before/after the collision time.

3.3 DEM simulation setup

The simulations were set up to mimic the experiments. The material properties for the spheres and liquid used are shown in Table 1. A half step velocity Verlet scheme was used to integrate Newton's equations of motion (Eq. 4 & Eq. 5) with a time step of 1×10^{-8} s. The Rayleigh and Hertz time were calculated and found to be on the order of $\times10^{-5}$. Previous work has indicated that the minimum time step for simulation of a wet granular flow should be two orders of magnitude smaller than either the Rayleigh or Hertz time, so a conservative time step of 1×10^{-8} s was used [28]. The positional, force, and velocity data for the

Table 1: Material properties for the solid spheres and interstitial liquid used in the DEM simulations.

Parameter	Value
Radius, r_i (mm)	12.7
Density, ρ (kg/m^3)	7960
Young's Modulus, E (Pa)	2.0×10^{11}
Poisson's Ratio, ν	0.35
Dry coefficient of restitution, e_{dry}	0.9
Viscosity, μ (Pa.s)	10
Surface tension, σ (N/m^2)	0.0205

spheres are output every $1{\times}10^{-5}$ s. Collisions with $St^n > 0.6$ are simulated for a total time of 0.2 s, while collisions with $St^n \leq 0.6$ are simulated for a total time of 1 s. The collision is considered finished when F_x & $F_y = 0$ or the spheres have completed a full rotation about each other. The forces applied on the spheres are dependent on the distance between the spheres, as given by Eq. 7–Eq. 10. In LIGGGHTS^{TM} this is represented by two functions: SurfacesClose, for when the surfaces are near and the liquid film is in contact with a sphere, and SurfacesIntersect, for direct overlap of the solid surfaces of the spheres. In this study, SurfacesClose considers all forms of the viscous force equations outlined by Eq. 12 and Eq. 13. Whilst, SurfacesClose will only consider the viscous force cases when $h_{min} > h_{ij}$ in Eq. 12 and Eq.13.

4 Results

First, experimental measurements are presented for a single stationary particle coated in 10 Pa.s silicone oil and contacted by a dry striker sphere at different contact angles and striking velocities. These experimental measurements are then compared with simulations performed using viscous and capillary force models.

4.1 Experimental oblique collisions

Fig. 6 shows the change in e^n with increasing St^n and collision angle. From Fig. 6 it can be seen that there are three distinct regions: low St^n where e^n is ≈ 0, medium St^n where e^n is a function of θ and very slightly increases with increasing St^n, and high St^n where e^n is only a function of St^n and contact angle is negligible. These results follow the sames trends first observed by Donahue et al. [21]. At low St^n, such that $e^n \approx 0$, the inertia of the particle is not sufficient to overcome the viscous and capillary forces within the measurement time of the experiment. As St^n increases to $St^n = 1$, the collisions enter the stick-rotate region. In the stick-rotate region, there are sufficient tangential inertial forces to initiate rotation, but they are not so sufficient that the spheres separate. For St^n in the range, $1.3 < St^n < 1.6$, the centrifugal forces during rotation are sufficient to separate the spheres. This is the stick-rotate-separate region. As St^n increases

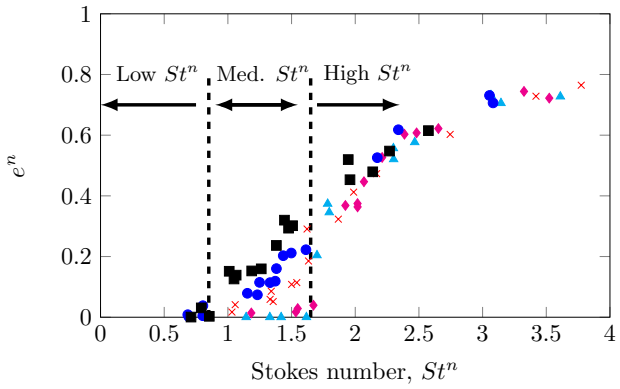

Figure 6: A comparison of the normal coefficient of restitution, e^n, versus normal Stokes number, St^n, for angled collisions of stainless steel spheres. The stationary sphere has $h^0_{1-2} = 270$ μm. The collision angles considered are 60°(■), 45°(●), 30°(×), 15°(◆), and 0°(▲).

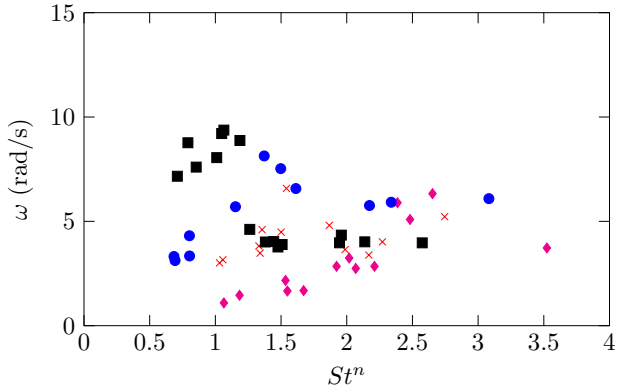

Figure 7: A comparison of the post-collisional rotational velocity versus normal Stokes number for angled collisions of stainless steel spheres. The stationary sphere has $h^0_{1-2} = 270$ μm. The collision angles considered are 60°(■), 45°(●), 30°(×), 15°(◆), and 0°(▲).

further, the collisions enter the contact-bounce region ($St^n > 1.6$). In the contact-bounce region, the data all collapse onto a common curve and e^n is independent of θ, and only dependent on St^n. In this high St^n contact-bounce region, the normal inertial forces are sufficient such that they can overcome any viscous and capillary forces and a rebound is initiated. Throughout the contact-bounce region, the spheres collide and then rotate about themselves, but they do not rotate about each other.

Fig. 7 shows the post-collisional rotational velocity for the collisions presented in Fig. 6. There is more scatter and uncertainty in the measurement of ω, however some general trends can still be observed from these data. For all collision angles, ω increases with increasing St^n up to some value and then suddenly declines. After this rapid decline, ω then slowly increases again with increasing St^n. The maximum value of ω before the decline increases with increasing θ. Furthermore, the critical St^n at which this peak ω occurs decreases with increasing collision angle θ. The post-collisional rotational velocity is likely determined by

the solid-solid contact and tangential viscous force. Hence, these data are valuable for validation of future tangential viscous force models.

4.2 Numerical simulation of oblique particle collisions

The discrete-element method was used to simulate the oblique collision of a stationary sphere with $h^0_{1-2} =$ 270 μm with a dry striker sphere at angles between 0° and 60°, as was measured in the experiments. For all the following numerical simulations the glass-transition pressure is experimentally fitted using the 0° case and then kept constant for all other collision angles. A similar approach was used in previous studies of oblique collisions[21, 26].

4.2.1 Comparison of Davis models to experimental results

Here we will compare the experimental data shown in Fig. 6 to a DEM model using Eq. 7 and Eq. 8 with the constant and near-constant viscous force conditions shown in Eq. 12 and Eq. 13. Initially we use the Davis tangential viscous force equation (Eq. 9) and neglect capillary forces. The constant and near-constant viscous force conditions are only implemented with the respective constant or near-constant tangential viscous force equation. The comparison of these models to experimental data is shown in Fig. 8. From Fig. 8 it can be seen that there is relatively good agreement for all models at $St^n > 1.5$. Specifically, the models which implement $\vec{F}^n_{visc}$ & $\vec{F}^t_{visc} = 0$ if $h_{min} > h_{ij}$, Fig. 8(b) and (c), have the best agreement at the highest considered St^n. The best-fit glass-transition pressures, for the 0° data, for all models were different for each model and were between 2.6 MPa and 23 MPa. Higher P_{gt} values were needed when the viscous force was set to 0 for $h_{min} > h_{ij}$. A higher P_{gt} value corresponds to a smaller h_{min} value, to compensate for the shorter duration of time over which the viscous force is applied. The glass-transition pressure values obtained here are comparable to the values of 6 MPa and 22 MPa found in other work [23, 26].

For $St^n < 1.5$ and $\theta > 30°$, all models in Fig. 8 predict an elongated region of non-zero e^n which is not seen in the experiments. At low St^n and high θ, a collision can take upwards of 1 s to fully resolve, i.e. to reach F_x & $F_y = 0$. The fully resolved condition occurs when the centrifugal forces overcome the viscous/capillary forces and the spheres separate leading to the stick-rotate-separate phenomena. For low St^n collisions, we do not observe the stick-rotate-separate phenomena experimentally as the maximum experimental imaging time is ≈ 0.07 s before pendulum forces become significant. Fig. 9 shows a comparison of experimental data with the DB model with a maximum simulation time of 0.07 s. From Fig. 9 it can be seen that the elongated region at low St^n for high θ has been significantly reduced and the simulation predictions are now comparable to the experiments. Furthermore, we observe no change in e^n past the critical St^n where $e^n > 0$

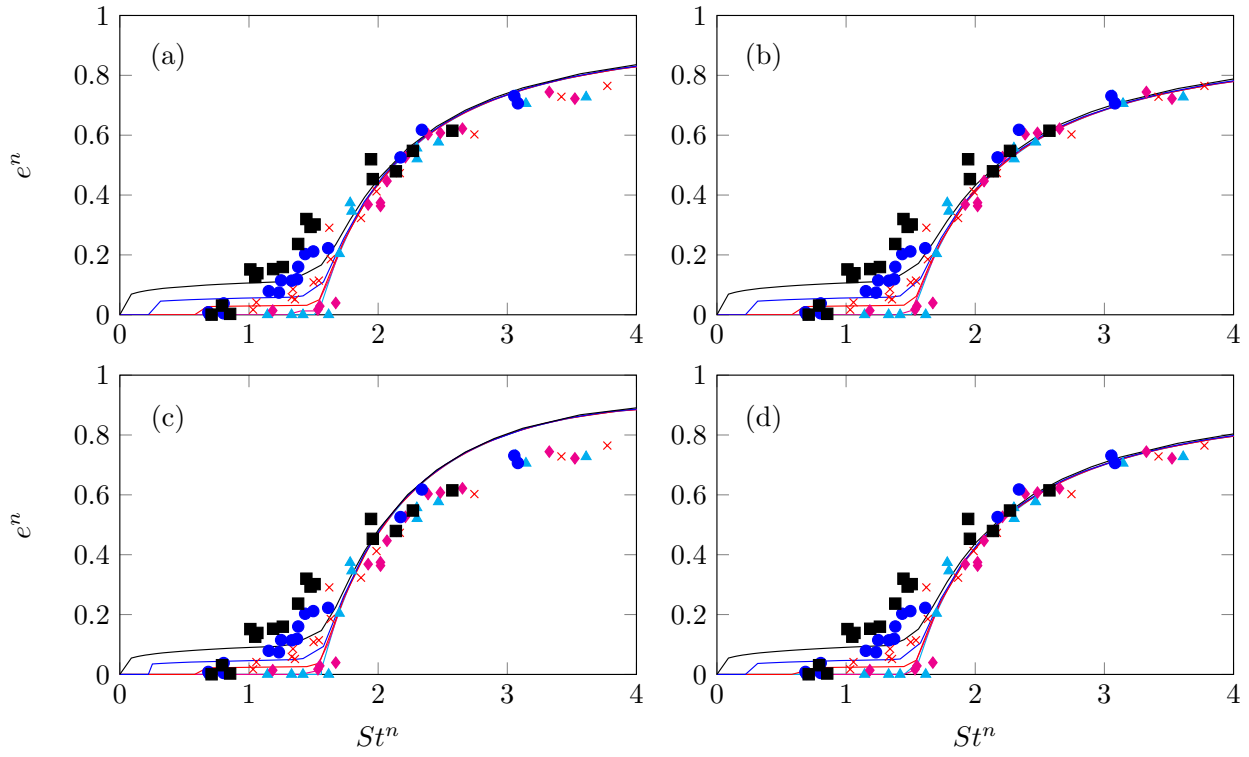

Figure 8: A comparison of experimental data and numerical simulations using the different Davis models. Experimental data is given by markers and simulation data is given by lines. The collision angles considered are 60°(■)(—), 45°(●)(—), 30°(×)(—), 15°(◆)(—), and 0°(▲)(—). (a) represents the Davis SB model with F^n_{visc} & $F^t_{visc} \neq 0$ when $h_{min} > h_{ij}$ at $P_{gt} = 4.9$ MPa , (b) represents the Davis SB model with F^n_{visc} & $F^t_{visc} = 0$ when $h_{min} > h_{ij}$ at $P_{gt} = 23$ MPa, (c) is the Davis DB model where F^n_{visc} & $F^t_{visc} \neq 0$ when $h_{min} > h_{ij}$ at $P_{gt} = 2.6$ MPa, and (d) is the Davis DB model where F^n_{visc} & $F^t_{visc} = 0$ when $h_{min} > h_{ij}$ at $P_{gt} = 11.6$ MPa.

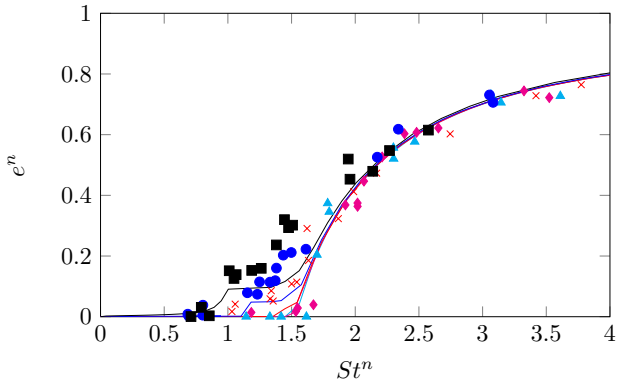

Figure 9: A comparison of experimental data to the Davis DB model where F^n_{visc}&$F^t_{visc} = 0$ if $h_{min} > h_{ij}$. Collisions are considered finished at $t = 0.07$ s and e^n is evaluated at this time. The model is given by the lines and the experimental data by the markers. The collision angles considered are 60°(■)(—), 45°(●)(—), 30°(×)(—), 15°(◆)(—), and 0°(▲)(—).

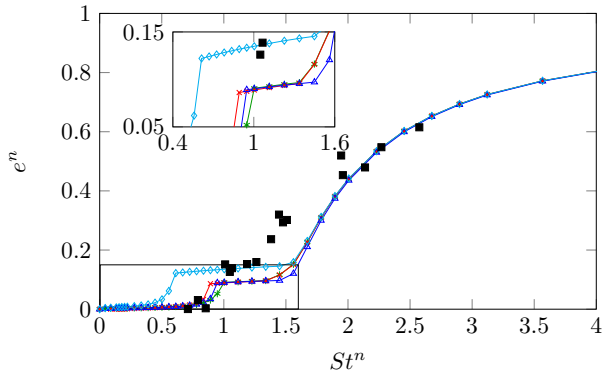

Figure 10: The coefficient of restitution for the Davis DB model with $F_{visc} = 0$ when $h_{min} > h_{ij}$ with different tangential viscous and/or capillary force models for a 60° collision. The simulations are considered finished at t = 0.07 s. The models considered are: no tangential viscous force model (⟡), Davis tangential viscous force model (✳), Nase tangential viscous force model (△), and the Davis tangential viscous force model with capillary force (✳). Experimental data is given by (■).

as the collisions are fully resolved by 0.07 s. It is likely that if it were not for experimental limitations, we would also observe a non-zero e^n at low St^n and high θ.

The results shown in Fig. 8 demonstrate that there is negligible difference between the SB model and the DB model when the criterion $\vec{F}^n_{visc}$ & $\vec{F}^t_{visc} = 0$ if $h_{min} > h_{ij}$ is implemented. The DB model considers the extension of the interstitial liquid due to squeezing forces and is considered more complete, and so the model in Fig. 8(d) is the only normal force model which will be considered in the rest of this study. Furthermore, the results shown in Fig. 8 and Fig. 9 are consistent with the results of Davis & Sitision, indicating the soft sphere model can be used to describe the collisions equally well [26].

4.2.2 Effect of capillary force and tangential viscous force

In this section we consider the effect of the capillary forces. Both the capillary force and viscous tangential force will be most significant when the collision angle θ is high. Therefore, only the 60° collisions are considered. The effect of the tangential viscous force and capillary force for the 60° collision at varying St^n is shown in Fig. 10. It can be seen that including a tangential viscous force model has a significant effect on the results between $0.4 < St^n < 1.6$. Furthermore, when tangential viscous forces are not considered the collision finishes significantly faster at lower St^n, i.e. the region with near-constant non-zero e^n is elongated to the left. There is no significant difference between the Davis and Nase models and it cannot be said which is more appropriate. A fully resolved plot of Fig. 10 has been provided in Appendix B.

At $St^n > 1.6$ the system transitions from the stick-rotate-separate region and enters the contact-bounce region. In the contact-bounce region, the effect of including a tangential force model is insignificant, indicating that tangential forces are negligible at high St^n due to the increased normal inertial force which dictates

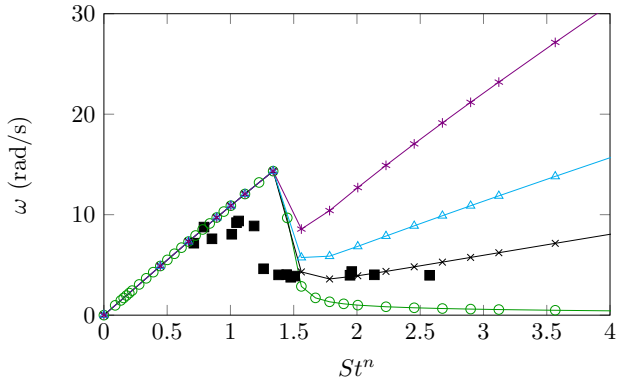

Figure 11: The post-collisional rotational velocity for 60° collisions and the Davis DB model with $F_{visc} = 0$ when $h_{ij} \geq h_{min}$ with varying coefficient of friction. The coefficients of friction considered are $\mu_f = 0$ (⊖), $\mu_f = 0.05$(✳), $\mu_f = 0.1$(△), and $\mu_f = 0.2$ (✳). Experimental data is given by (■).

whether or not bounce occurs.

4.2.3 Effect of coefficient of friction

The experiments shown in Fig. 7 indicate that the rotational velocity increases to a maximum and then decreases before increasing at high St^n. Here we examine the effect of friction by comparing simulations with different values for the coefficient of friction, μ_f, and experiments. Fig. 11 shows the effect of μ_f on ω. It can be seen that there is no change in ω with varying μ_f at low St^n. After ω peaks at some critical St^n ($St^n \approx 1.5$), ω rapidly decreases and then begins to increase with increasing St^n. By increasing μ_f, ω falls less after peaking, and also increases at a faster rate after falling. Similar qualitative results were obtained in the simulations of Davis & Sitison [26]. The results in Fig. 11 suggest that $\mu_f = 0.05$ shows fair agreement with the experimental data.

Fig. 12 shows ω post-collision for simulations using the DB model with the Davis tangential force model for all collision angles with $\mu_f = 0$ and $\mu_f = 0.05$. For low-medium St^n both models follow the trend seen experimentally — ω increases with increasing St^n up to a peak and then rapidly decreases. The maximum ω also increases with increasing angle, consistent with the experiments. The collisions at low St^n are all stick-rotate or stick-rotate-separate cases and there is no physical contact between the spheres; therefore, the coefficient of friction does not effect ω. However, at higher St^n, ω increases with increasing St^n for $\mu_f = 0.05$ whilst ω decreases with increasing St^n when $\mu_f = 0$. Interestingly, the $\mu_f = 0$ model predicts a near-zero ω once the collisions enter the contact-bounce region. The non-zero ω in the experiments at high St^n suggests that it is necessary to include a solid-solid friction model, even for these highly viscous systems. However, even including friction in the model, the critical value of St^n at which ω decreases is not predicted well. The experimental data suggests that as θ increases, this critical St^n should increase slightly. However,

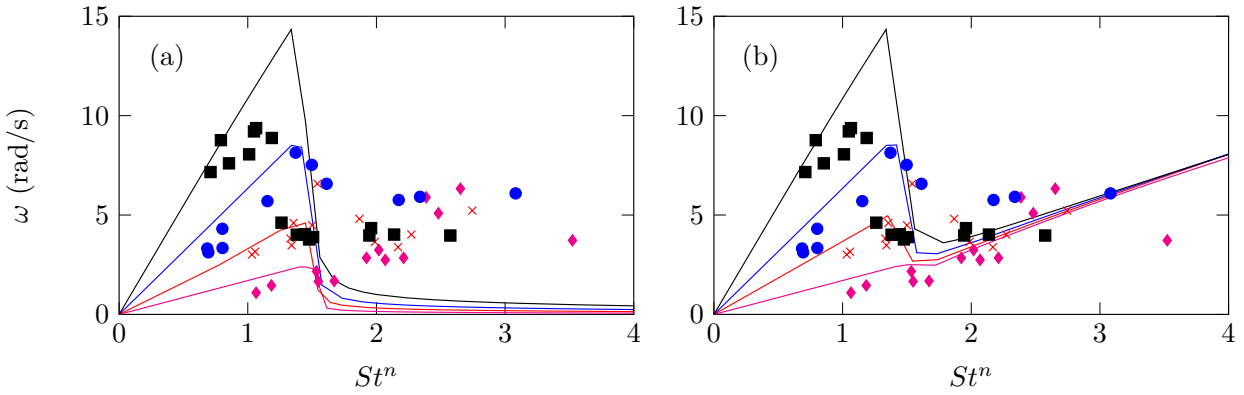

Figure 12: A comparison of the rotational velocity post-collision for experimental data and numerical simulations using the Davis DB model with (a) $\mu_f = 0$, and (b) $\mu_f = 0.05$. Experimental data is given by markers and simulation data is given by lines. The collision angles considered are 60°(■)(—), 45°(●)(—), 30°(×)(—), and 15°(◆)(—).

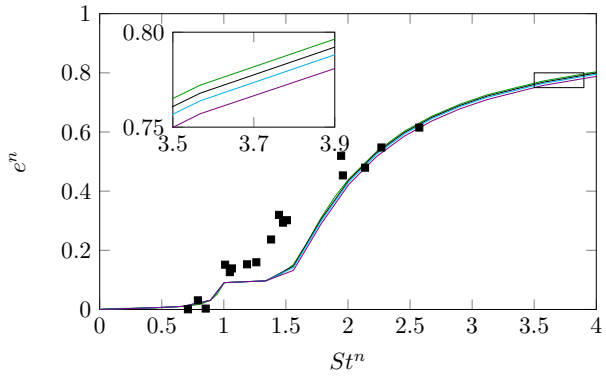

Figure 13: A comparison of St^n versus e^n for varying μ_f for a 60° collision. The coefficients of friction considered are: $\mu_f = 0$ (—), $\mu_f = 0.05$ (—), $\mu_f = 0.1$ (—), and $\mu_f = 0.2$ (—). Experimental data is given by (■)

the simulations do not predict any change in this critical St^n.

Fig. 13 shows the effect of μ_f on e^n for the 60° collision. Only the 60° collision is considered here as it will have the highest post-collisional rotational velocity, and therefore will be most affected by μ_f. The results show that e^n is independent of μ_f at low to medium St^n, as there is no physical contact occurring. For higher St^n, there is a slight dependence of e^n on μ_f, but the effect is insignificant.

Including μ_f results in better agreement for ω at high St^n, but has had insignificant effect on e^n. Specifically, the agreement at low–med St^n ($St^n < 1.5$) is still significantly poorer than at high St^n, regardless of the value of μ_f. This poorer agreement at low–med St^n indicates that changes must be made to the tangential viscous force equation to better describe this low–med. St^n ($St^n < 1.5$) region.

5 Conclusion

In this work the translational and rotational components of oblique collisions of spheres coated with thin viscous films have been measured. Comprehensive experimental data has been presented to help validate viscous force models. It was found that all of the tested viscous force models have fairly good agreement at high Stokes' number, when the collisions are dominated by the normal components and are independent of collision angle. The poorest agreement was seen for the DB model with $F_{visc} \neq 0$ if $h_{min} > h_{ij}$. However, the models fail to describe the low–medium Stokes' number regions where tangential forces dominate. There was found to be negligible improvement with the addition of capillary forces or a different tangential viscous force model (Nase). Furthermore, it is essential to include a frictional solid-solid contact model in order to describe the rotational velocity of the particles at high St^n accurately. These results suggest that the normal viscous force models are quite accurate for describing the wet particle collisions in the pendular regime. However, more work is needed to improve the tangential force models to describe the rotational velocity and normal coefficient of restitution for oblique collisions.

Appendix A. Derivation of rotation equations

First we consider a 2 by 2 rotation matrix, R, for rotation about the x plane, and y plane.

$$R = \begin{bmatrix} cos(\alpha) & -sin(\alpha) \\ sin(\alpha) & cos(\alpha) \end{bmatrix} \tag{24}$$

R can then be multiplied by any vector to rotate that vector by an angle, α. Here we use the distance between the central dot and outer dot to be rotated—we will refer to this as $\vec{D}$. Hence,

$$\vec{D} = \begin{bmatrix} p^i_{x,2} - p^i_{x,1} \\ p^i_{y,2} - p^i_{y,1} \end{bmatrix} \tag{25}$$

A small angle appromxiation of R is then made, where $sin(\alpha) = \alpha$ and $cos(\alpha) = 1$. Thus, R is now given by,

$$R = \begin{bmatrix} 1 & -\alpha \\ \alpha & 1 \end{bmatrix} \tag{26}$$

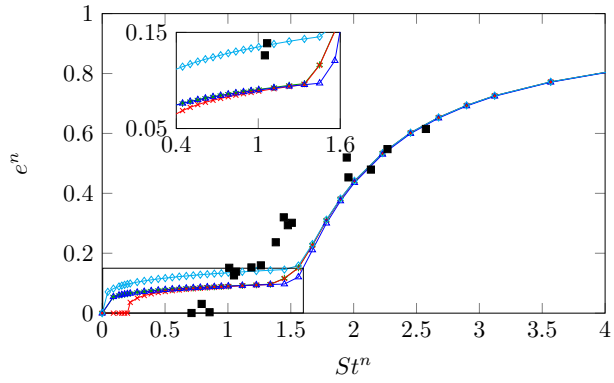

Figure 14: The coefficient of restitution for the Davis 2020 normal viscous force model with $F_{visc} = 0$ when $h_{ij} \geq h_{min}$ with different tangential viscous and/or capillary force models for a 60° collision. The models considered are: no tangential viscous force model (◇), Davis tangential viscous force model (✳), Nase tangential viscous force model (△), and the Davis tangential viscous force model with capillary force (✳). Experimental data is given by (■).

The change in position, due to rotation, for the x and y components of the outer dots is then given by $R\vec{D}$,

$$R\vec{D} = \begin{bmatrix} (p^i_{x,2} - p^i_{x,1}) - \alpha(p^i_{y,2} - p^i_{y,1}) \\ (p^i_{y,2} - p^i_{y,1}) + \alpha(p^i_{x,2} - p^i_{x,1}) \end{bmatrix} \tag{27}$$

The change in position of the outer dots considering both translational and rotational motion are then given by combining Eq. 17 or Eq. 18 with their respective parts of Eq. 27,

$$p^{i+1}_{x,2} = p^i_{x,1} + \vec{v}_x \Delta t + (p^i_{x,2} - p^i_{x,1}) - \alpha(p^i_{y,2} - p^i_{y,1}) \tag{28}$$

$$p^{i+1}_{y,2} = p^i_{y,1} + \vec{v}_y \Delta t + (p^i_{y,2} - p^i_{y,1}) + \alpha(p^i_{x,2} - p^i_{x,1}) \tag{29}$$

As α is given by $\omega \Delta t$, Eq. 28 and Eq. 29 can be simplified to give Eq. 19 and Eq. 20, respectively.

Appendix B. Fully resolved capillary force plot

Fig. 14 shows the fully resolved plot of e^n versus St^n for the different tangential force models. There are slight differences between the simulations when capillary forces are included at very low St^n ($St^n < 0.4$). However, these differences are negligible when $St^n \geq 0.4$, which is the region we could study experimentally.

References

[1] Kamrin, K. & Koval, G. Effect of particle surface friction on nonlocal constitutive behavior of flowing granular media. *Computational Particle Mechanics*. **1**, 169-176 (2014)

[2] Danczyk, M., Meaclem, T., Mehdizad, M., Clarke, D., Galvosas, P., Fullard, L. & , D. Influence of contact parameters on Discrete Element method (DEM) simulations of flow from a hopper: Comparison with magnetic resonance imaging (MRI) measurements. *Powder Technology*. **372** pp. 671-684 (2020)

[3] Kasper, J., Magnanimo, V., Dejong, S., Beek, A. & Jarray, A. Effect of viscosity on the avalanche dynamics and flow transition of wet granular matter. *Particuology*. **59** pp. 64-75 (2021)

[4] Tang, T., He, Y., Ren, A. & Wang, T. Experimental Study and DEM Numerical Simulation of Dry/Wet Particle Flow Behaviors in a Spouted Bed. *Industrial & Engineering Chemistry Research*. **58**, 15353-15367 (2019)

[5] Andreotti, B., Forterre, Y. & Pouliquen, O. Granular media: between fluid and solid. (Cambridge University Pres,2013)

[6] Pahtz, T., Duran, O., Deklerk, D., Govender, I. & Trulsson, M. Local Rheology Relation with Variable Yield Stress Ratio across Dry, Wet, Dense, and Dilute Granular Flows. *Phys. Rev. Lett.*. **123** pp. 048001 (2019)

[7] Nase, S., Vargas, W., Abatan, A. & Mccarthy, J. Discrete characterization tools for cohesive granular material. *Powder Technology*. **116**, 214-223 (2001)

[8] Anand, A., Curtis, J., Wassgren, C., Hancock, B. & Ketterhagen, W. Predicting discharge dynamics of wet cohesive particles from a rectangular hopper using the discrete element method (DEM). *Chemical Engineering Science*. **64**, 5268-5275 (2009)

[9] Washino, K., Tan, H., Hounslow, M. & Salman, A. A new capillary force model implemented in micro-scale CFD DEM coupling for wet granulation. *Chemical Engineering Science*. **93** pp. 197-205 (2013)

[10] Umer, M. & Siraj, M. DEM studies of polydisperse wet granular flows. *Powder Technology*. **328** pp. 309-317 (2018)

[11] Zhang, H. & Li, S. DEM simulation of wet granular-fluid flows in spouted beds: Numerical studies and experimental verifications. *Powder Technology*. **318** pp. 337-349 (2017)

[12] Schmelzle, S. & Nirschl, H. DEM simulations: Mixing of dry and wet granular material with different contact angles. *Granular Matter*. **20**, 1–13 (2018)

[13] Mitarai, N. & Nori, F. Wet granular materials. *Advances In Physics*. **55**, 1-45 (2006)

[14] Washino, K., Chan, E., Matsumoto, T., Hashino, S., Tsuji, T. & Tanaka, T. Normal viscous force of pendular liquid bridge between two relatively moving particles. *Journal Of Colloid And Interface Science*. **494** pp. 255-265 (2017)

[15] Cho, J., Lu, N., Howard, M., Adams, R. & Datta, S. Crack formation and self-closing in shrinkable, granular packings. *Soft Matter*. **15** pp. 4689-4702 (2019)

[16] Donahue, C., Hrenya, C., Davis, R., Nakagawa, K., Zelinskaya, A. & Joseph, G. Stokes' cradle: normal three-body collisions between wetted particles. *Journal Of Fluid Mechanics*. **650** pp. 479-504 (2010)

[17] Davis, R. Simultaneous and sequential collisions of three wetted spheres. *Journal Of Fluid Mechanics*. **881** pp. 983-1009 (2019)

[18] Donahue, C., Davis, R., Kantak, A. & Hrenya, C. Mechanisms for agglomeration and deagglomeration following oblique collisions of wet particles. *Phys. Rev. E*. **86** pp. 021303 (2012)

[19] Davis, R., Serayssol, J. & Hinch, E.J. The elastohydrodynamic collision of two spheres. *Journal of Fluid Mechanics*. **163**, 479–497 (1986)

[20] Buck, B., Tang, Y., Heinrich, S., Deen, N. & Kuipers, J. Collision dynamics of wet solids: Rebound and rotation. *Powder Technology*. **316** pp. 218-224 (2017)

[21] Donahue, C., Brewer, W., Davis, R.& Hrenya, C. *Journal Of Fluid Mechanics*. **708**

[22] Kantak, A. & Davis, R. Oblique Collisions and Rebound of Spheres from a Wetted Surface. *Journal Of Fluid Mechanics*. **509.** 63-81 (2004)

[23] Danczyk, M., Punch, O., Fullard, L., Hawken, M. & , D. A comparison of models of linear collisions between spherical particles in the pendular regime. *Powder Technology*. **398** pp. 117112 (2022)

[24] Hocking, L. The effect of slip on the motion of a sphere close to a wall and of two adjacent spheres. *Journal Of Engineering Mathematics*. **7**, 207-221 (1973)

[25] Reynolds, O. IV. On the theory of lubrication and its application to Mr. Beauchamp Tower's experiments, including an experimental determination of the viscosity of olive oil. *Philosophical Transactions Of The Royal Society Of London*. **177** 157-234 (1886)

[26] Davis, R. & Sitison, J. Oblique collisions of two wetted spheres. *Phys. Rev. Fluids.* **5** pp. 054305 (2020)

[27] Easo, L. Liquid dispersion in sheared particulate material.

[28] Washino, K., Chan, E., Miyazaki, K., Tsuji, T. & Tanaka, T. Time step criteria in DEM simulation of wet particles in viscosity dominant systems. *Powder Technology.* **302** pp. 100-107 (2016)

[29] Buck, B. & Heinrich, S. Collision dynamics of wet particles: Comparison of literature models to new experiments. *Advanced Powder Technology.* **30**, 3241-3252 (2019)

[30] Kloss, C., Goniva, C., Hager, A., Amberger, S. & Pirker, S. Models, algorithms and validation for opensource DEM and CFD-DEM. *Progress In Computational Fluid Dynamics, An International Journal.* **12**, 140-152 (2012)

[31] Kantak, A. & Davis, R. Elastohydrodynamic theory for wet oblique collisions. *Powder Technology.* **168**, 42-52 (2006)

[32] O'neill, M. A Slow motion of viscous liquid caused by a slowly moving solid sphere. *Mathematika.* **11**, 67-74 (196)

[33] Goldman, A., Cox, R. & Brenner, H. Slow viscous motion of a sphere parallel to a plane wall—I Motion through a quiescent fluid. *Chemical Engineering Science.* **22**, 637-651 (1967)